

Article

Quantification of the Effective Detectable Period for Concrete Voids of CLP by Lock-In Thermography

Chunyoung Kim ¹, Seongmin Kang ¹, Yoonjae Chung ², Okhwan Kim ³ and Wontae Kim ^{2,*} 

¹ enesG, 8, Techno 10-ro, Yuseong-gu, Daejeon 34026, Republic of Korea; chunyoung.kim@enesg.co.kr (C.K.); seongmin.kang@enesg.co.kr (S.K.)

² Eco-Sustainable Energy Research Institute, Kongju National University, 1223-24 Cheonan-daero, Seobuk-gu, Cheonan-si 31080, Republic of Korea; dbswosla79@kongju.ac.kr

³ Division of Mechanical & Automotive Engineering, Kongju National University, 1223-24 Cheonan-daero, Seobuk-gu, Cheonan-si 31080, Republic of Korea; owkim@kongju.ac.kr

* Correspondence: kwt@kongju.ac.kr; Tel.: +82-41-521-9380

Abstract: This study is to inspect the voids between the concrete containment building and the containment liner plate (CLP) in the light-water reactor type nuclear power plant with lock-in thermography (LIT) inspection technology. For that, a finite element method (FEM) model containing concrete voids was created, and the thermal distribution change of the CLP surface was simulated through numerical analysis simulation of various LIT inspection conditions and converted with real-time thermography data. For the simulated temperature distribution image and the amplitude and phase images calculated by the four-point method, the signal-to-noise ratio (SNR) is analyzed based on the sound area and void areas. As a result, the difference in SNR according to the size of voids was remarkable, and the effective detectable period (EDP), which was common to each inspection condition, was derived. Furthermore, a CLP concrete mockup identical to the model shape is produced, and the thermal image of the EDP is analyzed through the experiment with the same analysis technique, and the results are compared. Although there are some differences between the numerical analysis conditions and the experimental environments, the deduction and utilization of EDP through FEM simulation are considered useful approaches to applying LIT to inspect concrete voids on the back of the CLP.



Citation: Kim, C.; Kang, S.; Chung, Y.; Kim, O.; Kim, W. Quantification of the Effective Detectable Period for Concrete Voids of CLP by Lock-In Thermography. *Appl. Sci.* **2023**, *13*, 8247. <https://doi.org/10.3390/app13148247>

Academic Editor: Giuseppe Lacidogna

Received: 2 June 2023

Revised: 6 July 2023

Accepted: 13 July 2023

Published: 16 July 2023



Copyright: © 2023 by the authors. Licensee MDPI, Basel, Switzerland. This article is an open access article distributed under the terms and conditions of the Creative Commons Attribution (CC BY) license (<https://creativecommons.org/licenses/by/4.0/>).

1. Introduction

Non-destructive testing (NDT) is a method to check the state and soundness of equipment and facilities without destroying or transforming them. This technology is designed to prevent accidents in equipment and facilities and is performed according to various requirements and standards for safety and reliability [1,2].

Thermography testing (TT) is one of the advanced NDT technologies that can quickly and non-contactly inspect a large area. Recently, research on the development of flaw detection techniques and devices to apply thermography to various industries and objects has been actively conducted [3–13].

The concrete containment building of a light-water reactor-type nuclear power plant includes several levels of containment structures. The concrete outer wall of the containment building and the inner containment liner plate (CLP) are both important containment structures. CLP serves as a formwork for concrete casting when constructing a containment building and as a pressure vessel to protect internal equipment and prevent leakage of radioactive materials during power plant operations and emergencies. When manufacturing the CLP, various structures and additives are bonded to the inside and outside of the CLP. Such a structure may cause mortar flow failure when constructing a containment building.

The problem of multiple voids forming between the CLP and the outer wall of the concrete was confirmed through a recent inspection report [14,15].

Unlike the painted surface, concrete voids cause corrosion on the back of the CLP and, in an emergency, can cause a decrease in the strength of the CLP and concrete containment building. Therefore, it is considered possible to secure the designed function in case of emergency and to promote the stable operation of the containment building by allowing the concrete void on the back of the CLP to be checked in advance through NDT.

Currently, the inspection of the concrete voids of the CLP and the back surface is carried out by selective NDT methods such as visual inspection, ultrasonic thickness measurement, and impact sound testing for parts with a high possibility of some voids. If a technology that can detect the voids on the back of the CLP using infrared thermography technology is implemented, it is expected that a faster and easier inspection will be possible.

This study is about the LIT based on the inspection technique for the concrete voids on the back of the CLP. In the CLP structure of a nuclear power plant containment building, considering the connection situation between the metal plate and the concrete, it can be regarded as a composite structure. Various TT flaw detection techniques exist but LIT monitors the time dependence between the output and input signals caused by a defect. Therefore, LIT was chosen because it would be more advantageous to detect/identify/quantitatively evaluate various defects in composites.

For this, thermography simulation through the finite element method (FEM) model and numerical analysis, setting the effective detectable period (EDP) through the signal to noise ratio (SNR), and detection performance analysis and comparison using mockups are performed. Although this takes a lot of time and processing, a more accurate evaluation time can be set, and the accuracy of TT can be reconsidered. Compared to visual inspection or ultrasonic inspection, TT can more easily detect concrete voids on the back side of CLP and will be a useful method for the complete inspection of nuclear power plant containment buildings.

2. Theory

2.1. Lock-In Thermography (LIT)

Among the TT technologies, the LIT technique, which utilizes external energy, applies a heat load in the form of a controllable harmonic function to the inspection object and measures the temperature change formed on the surface of the inspection object with an infrared (IR) camera. It is a technique that demodulates the amplitude and phase changes of the measured data and compares and analyzes the difference to check for the existence of defects [16].

The LIT technique utilizes thermal changes caused by periodic excitation rather than instantaneous thermal changes, so it can detect minute differences in defects in the inspection target and has the effect of reducing external influences such as uneven heat load or emissivity.

2.2. Four-Point Method

Figure 1 shows the principle of data extraction and amplitude and phase calculation by the ‘4-point method’ for the thermal excitation and thermal response of the LIT [17]. The 4-point method utilizes thermal signals from three-time points (S_2 , S_3 , and S_4) of equal terms and a reference time point (S_1). For each pixel of each temperature image, by the following Equations (1) and (2), the amplitude and phase are calculated, and the result is a method of expressing a two-dimensional amplitude and phase image [17–21].

$$A\{x, y\} = \sqrt{(S_1 - S_3)^2 + (S_2 - S_4)^2} \quad (1)$$

$$\phi\{x, y\} = \tan^{-1}\left(\frac{S_1 - S_3}{S_2 - S_4}\right) \quad (2)$$

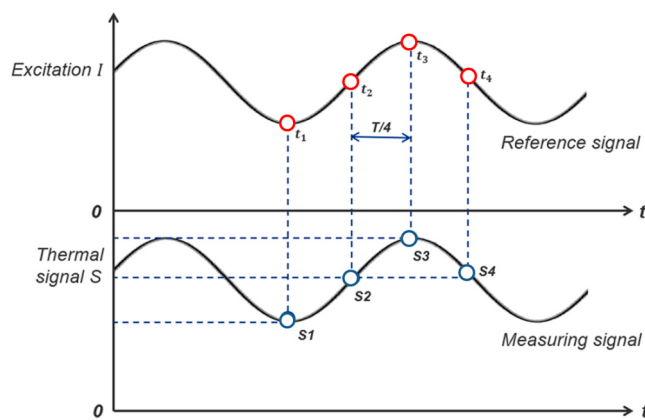


Figure 1. Principle of amplitude and phase calculation by the 4-point method [18].

In this study, all temperature images of the transient state are described by frame units, and the amplitude (A) and phase (ϕ) images are expressed in step units based on the S_1 time point.

2.3. LIT Heat Transfer

Heat transfer by external heat addition in LIT inspection can be explained as a physical nonlinear problem. The heat transfer at each node of the FEM thermal analysis model depends on the temperature, and the basic equation on the 3-axis Cartesian coordinates derived by Fourier's law can be expressed as Equation (3) [22].

$$k \left(\frac{\partial T}{\partial x} + \frac{\partial T}{\partial y} + \frac{\partial T}{\partial z} \right) = -q + h_{conv} (T - T_{0C}) + \sigma \varepsilon (T^4 - T_{0R}^4) \quad (3)$$

where k is the heat transfer coefficient of the material, q is the heat applied from the outside, h_{conv} is the convective heat transfer coefficient, σ is the Stefan–Boltzmann constant, ε is the emissivity of the surface, T is the temperature of the material, T_{0C} is the initial environmental temperature in convection, and T_{0R} is the initial environmental temperature in radiation.

The external heat q applied in LIT inspection can be expressed as a periodic excitation, as shown in Equation (4).

$$q = Q (\sin \omega t) \quad (q \geq 0) \quad (4)$$

where Q is the peak power during the periodic thermal addition period and ωt represents the phase angle.

These basic equations can be solved for known initial and boundary conditions, where the initial conditions take the form of the initial temperature distribution, while the boundary and load conditions can take the form of a specific temperature, a specific heat flux, convective conditions, radiant temperatures, etc. In FEM, Equation (3) is discretized for each node, and a matrix equation that is solved for an unknown temperature at any time is generated [23].

2.4. Signal-to-Noise Ratio (SNR)

In NDT, the ratio of the defect signal to the ambient noise is the SNR , which is a suitable factor for expressing the signal strength, uncertainty, and detectability [24]. As shown in Equation (5) below, the SNR value can be calculated as the signal strength ratio of the 'defective part (P_S)' to the 'sound part (P_N)' without defects and is expressed in

decibel (dB) units. In this case, when the signal strength level between the defective parts is doubled or halved, the difference in SNR value represents +6 dB or -6 dB.

$$SNR = 20 \log \left(\frac{P_S}{P_N} \right) \quad (5)$$

3. FEM Modeling and LIT Simulation

3.1. CLP Mockup Specimen

As shown in Figure 2, the shape of the mockup specimen considering the concrete void on the back of the CLP included four concrete voids of two areas ($75 \times 75 \text{ mm}^2$ and $105 \times 105 \text{ mm}^2$) and two depths (15 mm and 30 mm). All voids were designed to be located within an area of $250 \times 250 \text{ mm}^2$ in consideration of the inspection range of an IR camera (FLIR SC645). A 6 mm thick SS 275 plate similar to CLP was attached to the front of the concrete block, and black paint with an emissivity of 0.95 was applied to the surface of the plate.

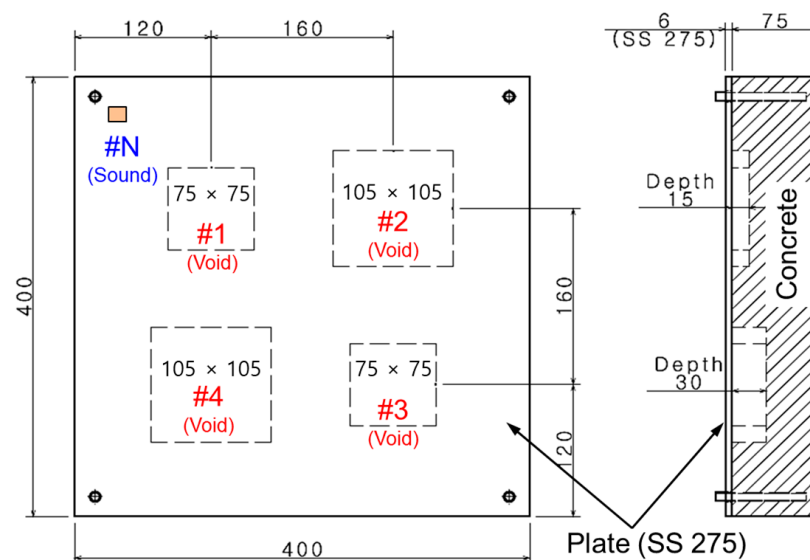


Figure 2. CLP mockup design with concrete voids (units: mm).

For the LIT simulation through numerical analysis and the analysis of the experimental results, identification numbers (#1 to #4) were assigned to each void part, and ‘sound parts’ without voids were distinguished by ‘#N’. In addition, ‘S’ for simulation and ‘E’ for mockup experiment are added to distinguish them.

3.2. FEM Model

The commercial software SpaceClaim 2022 R1 and ANSYS Workbench 2022 R1 were used to generate the FEM model and perform thermal analysis to be used for the LIT simulation, and the designed shape in Figure 2 was applied. Figure 3a is a 3D model created by SpaceClaim, and Figure 3b is an image of the finite element mesh shape created by ANSYS viewed from the front of the CLP. The element size of the model was set from a minimum of 2.5 mm to a maximum of 5 mm, and the grid of the CLP surface to perform the LIT simulation was fixed to 2.5 mm in both width and length and had three elements in the thickness direction.

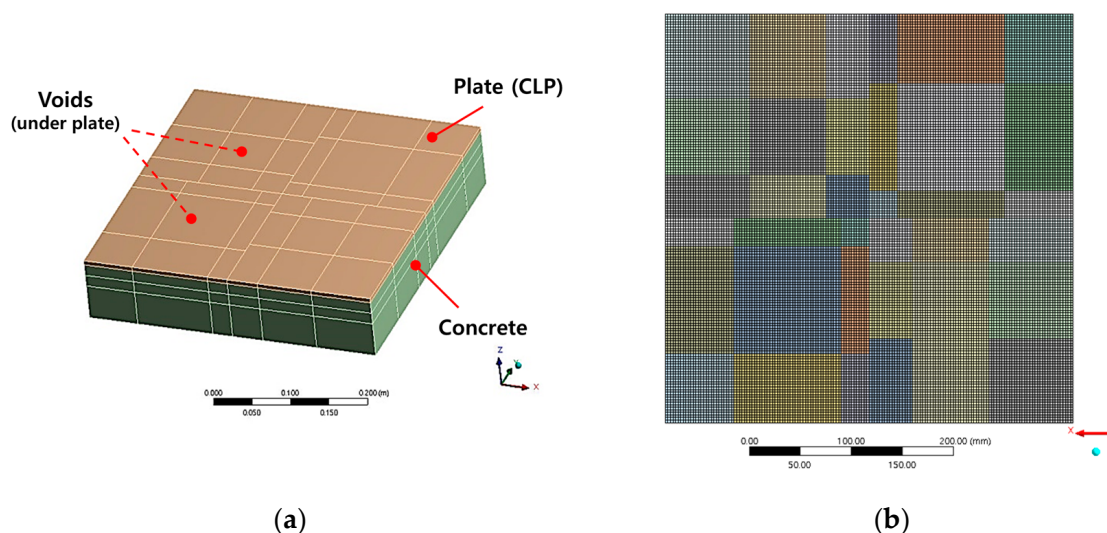


Figure 3. FEM model and plate mesh image: (a) FEM model with implied voids and (b) mesh image of the CLP front surface.

As a result of model meshing, 827,054 nodes and 177,660 elements were formed, and the CLP surface had a total of 25,921 nodes in a square lattice arrangement of 161×161 . In addition, #1 and #3 void surfaces have 31×31 nodes, and #2 and #4 void surfaces have 43×43 nodes. Table 1 shows the size and material properties of each component.

Table 1. Material properties and size of the CLP mockup.

| Properties | Unit | CLP | Concrete | Voids |
|----------------------|-----------------------------------|---------------------------|----------------------------|--|
| Volume | mm^3 | $400 \times 400 \times 6$ | $400 \times 400 \times 75$ | #1: $75 \times 75 \times 15$ #2: $105 \times 105 \times 15$ #3: $75 \times 75 \times 30$ #4: $105 \times 105 \times 30$ |
| Mass | kg | 7 | 26 | - |
| Thermal conductivity | $\text{W}/\text{m K}$ | 60.4 | 0.72 | 0.026 |
| Specific heat | $\text{J}/\text{kg}\cdot\text{K}$ | 496 | 780 | 1007 |
| Density | kg/m^3 | 7820 | 2300 | 1.16 |

3.3. Condition of LIT Simulation

In order to implement various LIT inspection conditions for the concrete voids on the back of the CLP, as shown in Table 2, four cases (Cases 1 to 4) were simulated at two levels for heat flux and frequency, respectively. The real-time temperature change and distribution of the CLP surface for each case can be predicted through the thermal distribution analysis of FEM.

Table 2. LIT simulation case conditions.

| Case | Heat Flux (kW/m^2) | Frequency (Hz) | Frame Rate (fps) |
|--------|--------------------------------------|----------------|------------------|
| Case 1 | 1 | 0.01 | 0.5 |
| Case 2 | 1 | 0.02 | 1.0 |
| Case 3 | 2 | 0.01 | 0.5 |
| Case 4 | 2 | 0.02 | 1.0 |

In the LIT simulation through the FEM model, as shown in Figure 4, the LIT device consisting of an IR camera, a function generator, an amplifier, a PC for control and analysis, and halogen lamps was considered. Additionally, in order to induce high emissivity, the black paint application condition applied to the CLP surface was also considered. These assumptions are similar to the actual LIT inspection experiments on CLP mockup specimens. The LIT simulation of each case was performed by the FEM model, and the environmental conditions equally applied to all simulations are as follows. The heat transfer coefficient by natural convection of gas-state fluid is suggested as $5\text{--}25 \text{ W/m}^2 \text{ K}$ [25]. This study was conducted in a stable laboratory environment, and the minimum value of $5 \text{ W/m}^2 \text{ K}$ was set:

- (1) Initial temperature: 22°C ;
- (2) Emissivity (ε) 0.95 of the plate surface;
- (3) The convection coefficient is $5.0 \text{ W/m}^2 \text{ K}$;
- (4) Heat load of 3 cycles of a positive (+) half-sine wave as shown in Figure 5;
- (5) Frame rate is considered 50 times per cycle.

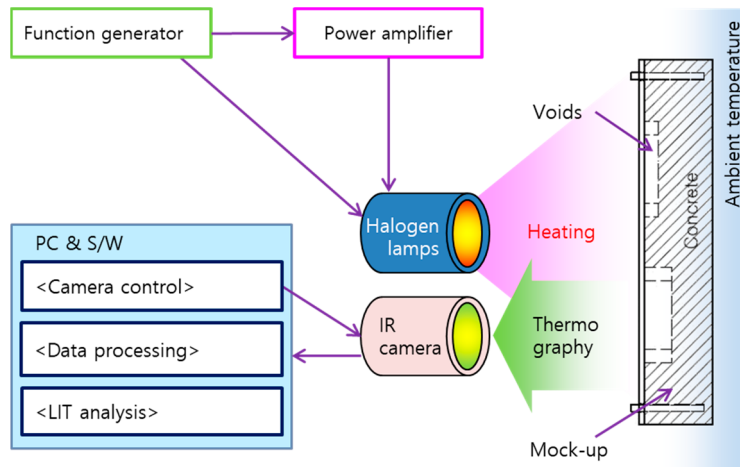


Figure 4. System configuration of LIT experiments.

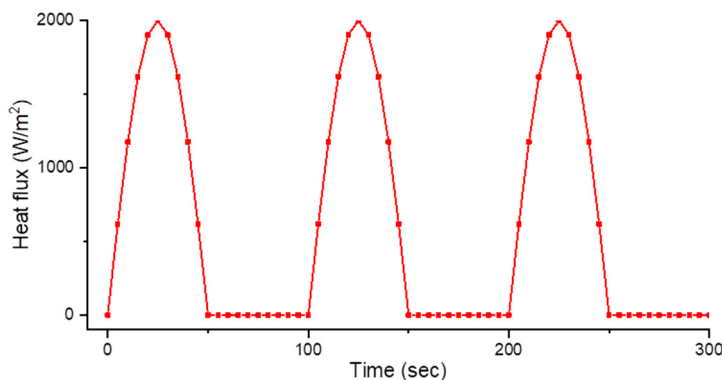


Figure 5. Timeline of heat flux over 3 cycles (ex. 0.01 Hz).

It was set so that 150 frames of thermography could be acquired for each case.

3.4. Node Map Construction

The LIT inspection technique is a technology that can be expected to detect relatively precise defects through the thermal change of the inspection target surface caused by an external periodic heat load. The LIT simulation derives the transient temperature distribution analysis result of the FEM model at a tight time interval of 50 frames per cycle. By extracting all the temperature values of 25,921 (161×161) nodes located on the CLP surface, which is the region of interest, for each frame, reconstructing them into a

two-dimensional sheet, and displaying them as images. Finally, the thermal analysis results of all frames can be converted into thermography. In order to extract and simulate these analysis results quickly and effectively, as shown in Figure 6, the ID number of each node was checked on the CLP surface of the FEM model, and a node map was constructed to match the spatial location and used for simulation.



Figure 6. Node map construction for data extraction and reconstruction (161×161 pixels).

3.5. LIT Thermography Replication

The temperature values for each frame were extracted from the LIT simulation results and reconstructed into a 161×161 pixel temperature image using MATLAB R2017b software and a node map. As an example, Figure 7a is the CLP surface temperature distribution image at 148 s derived from the LIT Simulation of Case 3, and Figure 7b is the #74 frame temperature image obtained by data extraction and reconstruction through the node map. The temperature image reconstructed for each case can be connected in chronological order and expressed as a single thermography. This has the effect of replicating the thermography data acquired by the IR camera in the actual LIT inspection experiment.

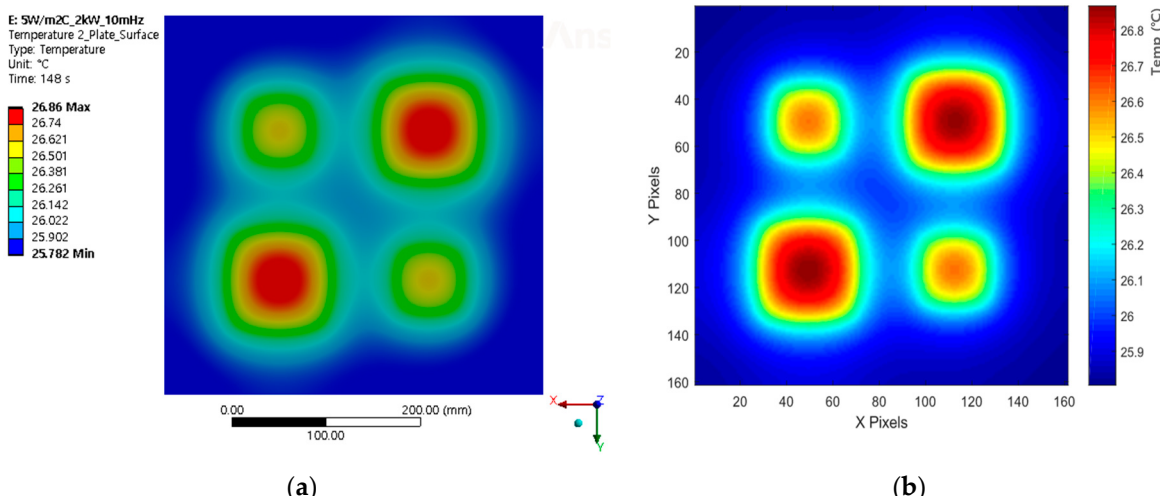


Figure 7. Temperature image by LIT simulation result in Case 3 (2 kW/m^2 , 0.01 Hz). (a) LIT simulated temperature distribution at 148 s and (b) reconstructed temperature image of #74 frame (at 148 s, by jet colormap).

3.6. LIT Defect Analysis Tool and EDP

For the replicated thermography data through the LIT simulation of each case, the 'LIT defect analysis tool' developed to quickly perform phase and amplitude image calculation and SNR analysis by the '4-point method' was applied [26]. This tool was developed using

MATLAB S/W, checks temperature images in frame units, calculates amplitude and phase images in step units, and, as shown in Figure 8, the SNR of the region of interest (ROI) by index (#NS and #1S to #4S) can be calculated, and the trend can be checked.

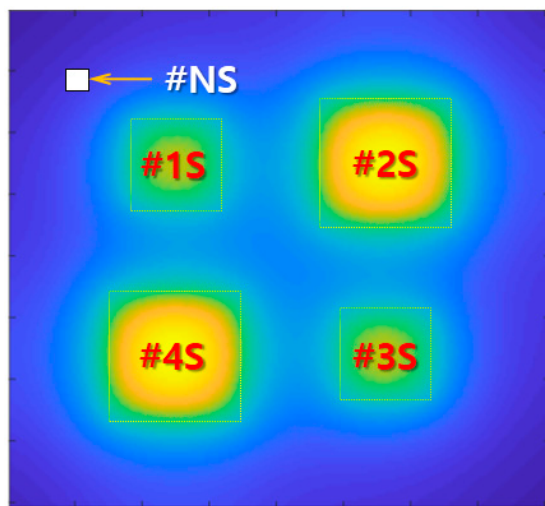


Figure 8. ROI indexing in the temperature image of the LIT simulation (161×161 pixels).

In this study, while the transient state changes in thermography data, the maximum SNR of the voids is more than ± 12 dB, and the period in which the SNR appears proportionally according to the size of the voids is defined as the ‘effective detectable period (EDP)’. During this period, the contrast between the healthy part and the defective part appears remarkable, and it can be seen that identification and detection of the defective part are easy in each thermogram. In addition, among the intervals common to the EDP of all cases, the comparative analysis time (by frame or step) was specified and used for evaluation and research.

4. CLP Mockup Test

4.1. Making of the CLP Mockup Specimen

According to the design and considerations in Section 3.1, a CLP mockup specimen was made as shown in Figure 9. An SS 275 plate was attached to the front of the concrete block containing 4 sizes of the void, and matte black paint was applied to the surface of the plate to secure an emissivity of 0.95.



Figure 9. CLP mockup specimen containing concrete voids.

4.2. Device Configuration and Experimental Method

The LIT test for the CLP mockup specimen is composed of an IR camera, a control PC, a function generator, an amplifying means, and a heating source, as shown in Figure 10. The IR camera used a FLIR SC645 model with a resolution of 640×480 pixels and a noise equivalent temperature difference (NETD) of 50 mK, and one or two halogen lamps with a maximum output of 1 kW were applied as the heating source. The distance between the front of the halogen lamps and the surface of the CLP mockup specimen was set to 1 m.

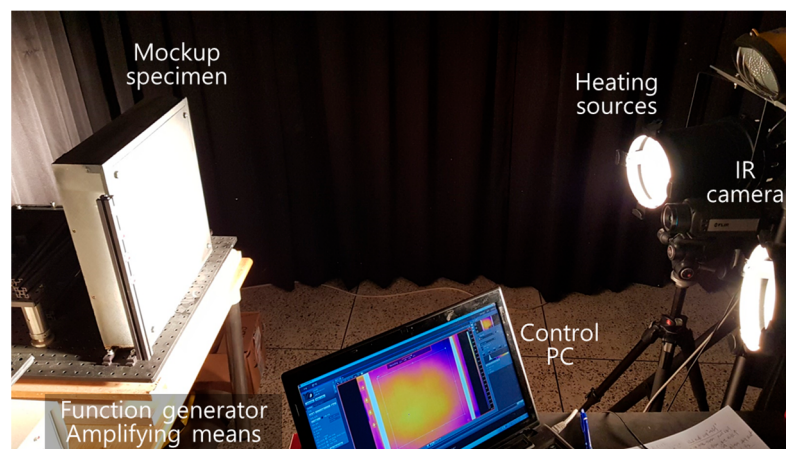


Figure 10. Picture of the experimental CLP mockup.

The experiment was conducted under four conditions based on the output of the halogen lamp and the heat addition frequency in an indoor darkroom environment (temperature: $24\text{ }^{\circ}\text{C}$ – $25\text{ }^{\circ}\text{C}$, humidity: 50–60%) without special air conditioning devices. The frequency, amplitude, and number of cycles of the heat source were controlled through a function generator so that a heat load of 3 cycles was applied in the form of a half-sine wave. Table 3 shows the experimental conditions performed on the CLP mockup specimen.

Table 3. CLP mockup experimental conditions.

| Condition | Lamp Power (kW) | Frequency (Hz) | Frame Rate (fps) |
|-----------|-----------------|----------------|------------------|
| Test 1 | 1 | 0.01 | 6.25 |
| Test 2 | 1 | 0.02 | 12.5 |
| Test 3 | 2 | 0.01 | 6.25 |
| Test 4 | 2 | 0.02 | 12.5 |

4.3. Analysis of Acquired Experimental Data

Figure 11a is a picture image displayed on the monitor in an actual experiment using 2 kW halogen lamps (2×1 kW lamps), and Figure 11b is a temperature image (640×480 pixels) expressing the measured temperature data in MATLAB. As shown in the picture, it can be assumed that the two lamps each have a hot spot, and the position of the hot spot reflected does not coincide with the center of the mockup specimen.

In the thermography of all frames observed through the experiment, the ‘LIT defect analysis tool’ according to the ‘4-point method’ was applied to an area of 480×440 pixels, excluding the outside part. Through this, a transient-state temperature image in frame units and phase and amplitude images in step units were calculated. In addition, as shown in Figure 12, the ROI index (#NE and #1E to #4E) is assigned to the same location as the simulation to check the SNR calculation and trend, which is then compared and explored with the simulation results.

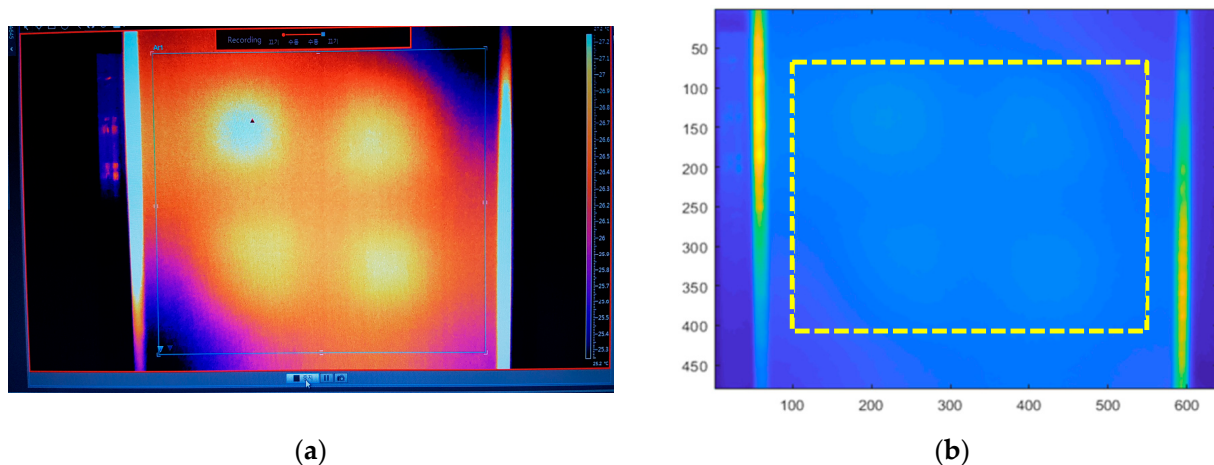


Figure 11. Acquired thermography of the CLP mockup experiment: (a) picture image of the PC monitor and (b) acquired temperature image by MATLAB S/W (640×480 pixels) and analysis area in yellow box (480×440 pixels).

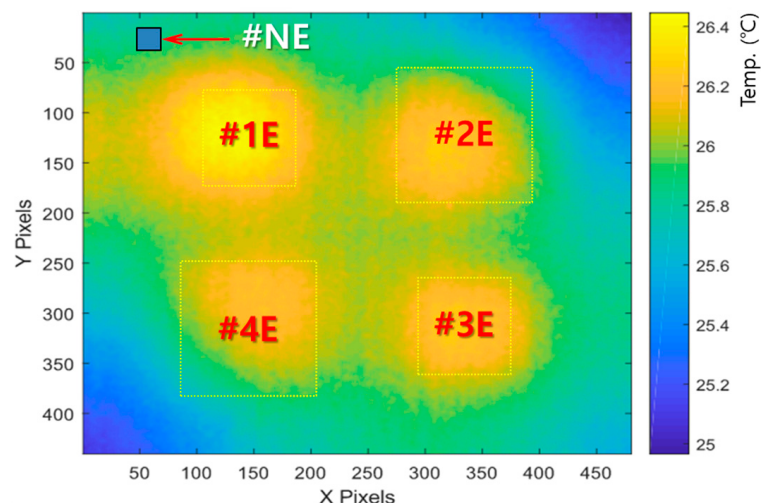


Figure 12. ROI indexing in an acquired temperature image (480×440 pixels).

The spatial resolution of the thermal image under the experimental conditions was 0.78 mm/pixel, and #1E and #3E voids each had a 96×96 pixel size, and #2E and #4E voids each had a 135×135 pixel size.

5. Results and Discussion

5.1. Analysis of Simulated Thermography and Deciding the EDP

The LIT defect analysis tool was applied to the thermography data of all cases replicated through simulation to analyze the SNR trend of temperature/amplitude/phase images in the transient state, and the EDP for each case was confirmed. Table 4 summarizes the EDP derived from the thermography data of each case, and Figure 13 is an example showing the temperature/amplitude/phase trend and SNR trend of the sound part and the void parts in Case 3. Figure 13b is the temperature SNR trend of each void, and the 12–151 frames satisfied the EDP condition. Figure 13d is the amplitude SNR trend, and the EDP was 1–12, 36–59, and 89–107 step sections. Figure 13f shows the phase SNR trend, and the EDP was met in the 3–5, 8–18, 57–69, and 106–115 step sections.

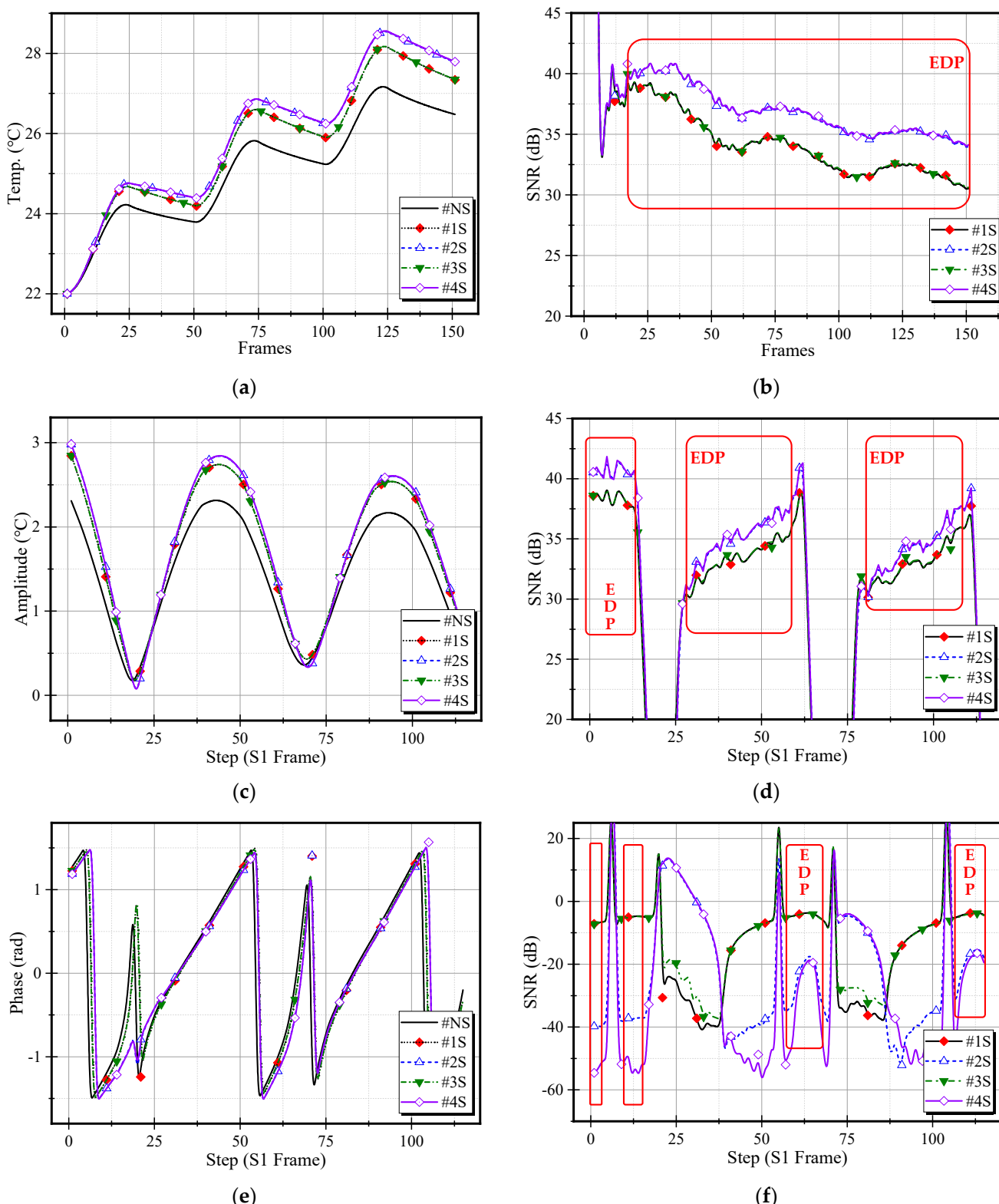


Figure 13. Analysis of simulated thermography and EDP (Case 3; 2 kW, 0.01 Hz): (a) temperature change; (b) temperature SNR trend; (c) amplitude change trend; (d) amplitude SNR trend; (e) phase change trend; and (f) phase SNR trend.

Table 4. EDP and comparative analysis time.

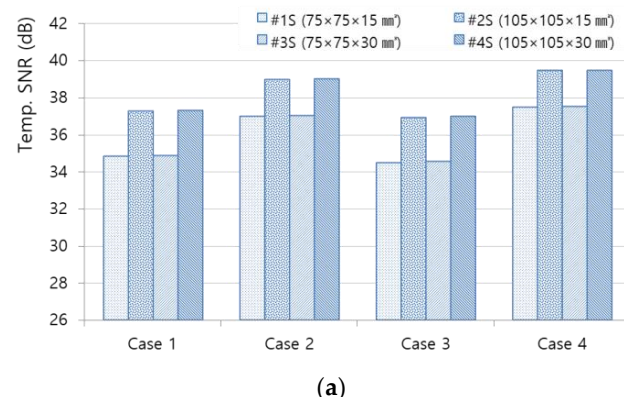
| Case | EDP | | |
|---------------|----------------------------|-------------------------|---|
| | Temperature SNR (Frame) | Amplitude SNR (Step) | Phase SNR (Step) |
| Case 1 | 27–151 | 1–15, 30–65, 82–111 | 8–18, 56–69, 106–115 |
| Case 2 | 23–151 | 1–12, 36–59, 89–107 | 20–28, 58–68, 102–104, 107–113 |
| Case 3 | 12–151 | 1–14, 28–62, 82–111 | 3–5, 8–18, 57–69, 106–115 |
| Case 4 | 16–151 | 1–17, 29–64, 81–113 | 4–6, 14–17, 20–28, 52–55, 58–69, 102–104, 107–115 |
| Analysis time | 74 (frame) | 58 (step) | 58 (step) |

Among the EDP common to all cases, the #74 frame for temperature and the #58 step for amplitude and phase were selected as mutual comparative analysis times. Considering the frame rate of each case, 0.01 Hz corresponds to the temperature at 148 s, the phase and amplitude at 116–141–166–191 s, and 0.02 Hz at 74 s and 58–70.5–83–95.5 s.

5.2. SNR Comparison of Simulated Thermography

A high SNR in thermography means that the contrast between the defective part and the healthy part is high, and it can be seen that the detection ability is high and flaw detection is easy. Identifying a specific shape or object in an image or video can generally be achieved by contrasting the surroundings and the signal. When this contrast is expressed in decibels through SNR calculation, arithmetically, ± 6 dB represents twice the signal strength between the surroundings and the object, and it is difficult to recognize a contrast close to 0 dB in human vision. The higher the SNR, the more advantageous the object recognition. As a quantitative evaluation method for the length or width of defects detected in various nondestructive testing techniques such as ultrasonic testing (UT), the 6 dB or 12 dB drop method is usefully used [27]. To use this technique in TT, it is considered that a contrast of at least 6 dB should be displayed.

Figure 14a–c shows the temperature, amplitude, and phase SNR for each case as a graph based on the selected comparative analysis time, and Figure 15a–c shows each thermal image of Case 3 as an example. As a result, a high contrast of more than 35 dB was shown in all cases, and it is judged that the detection of concrete voids on the back of the CLP will be smooth with the LIT inspection technique. In addition, in terms of SNR, the condition of 0.02 Hz was relatively higher than that of 0.01 Hz, and the effect of the difference in the void was large, but the effect of the difference in depth was very small.

**Figure 14. Cont.**

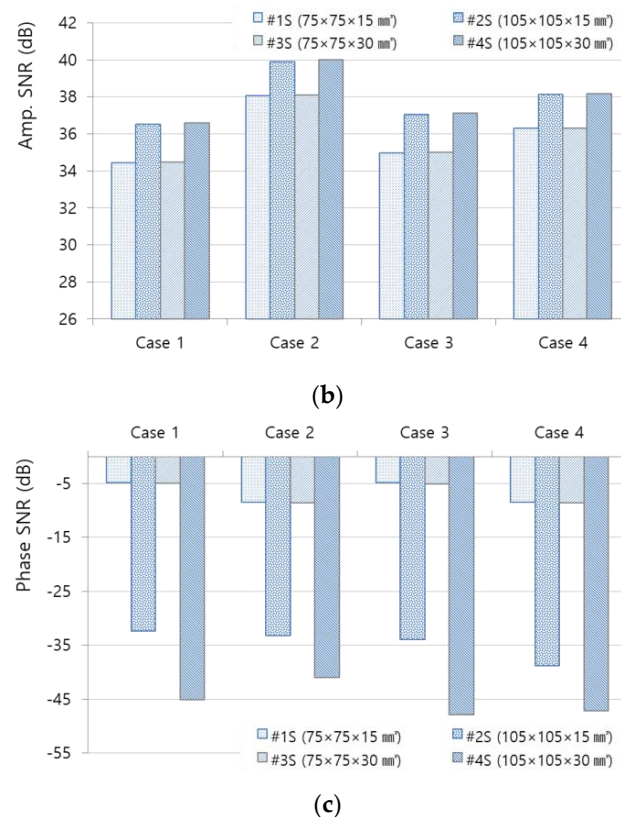


Figure 14. Comparison of LIT simulation results by case: (a) temperature SNR (#74 frame); (b) amplitude SNR (#58 step); and (c) phase SNR (#58 step).

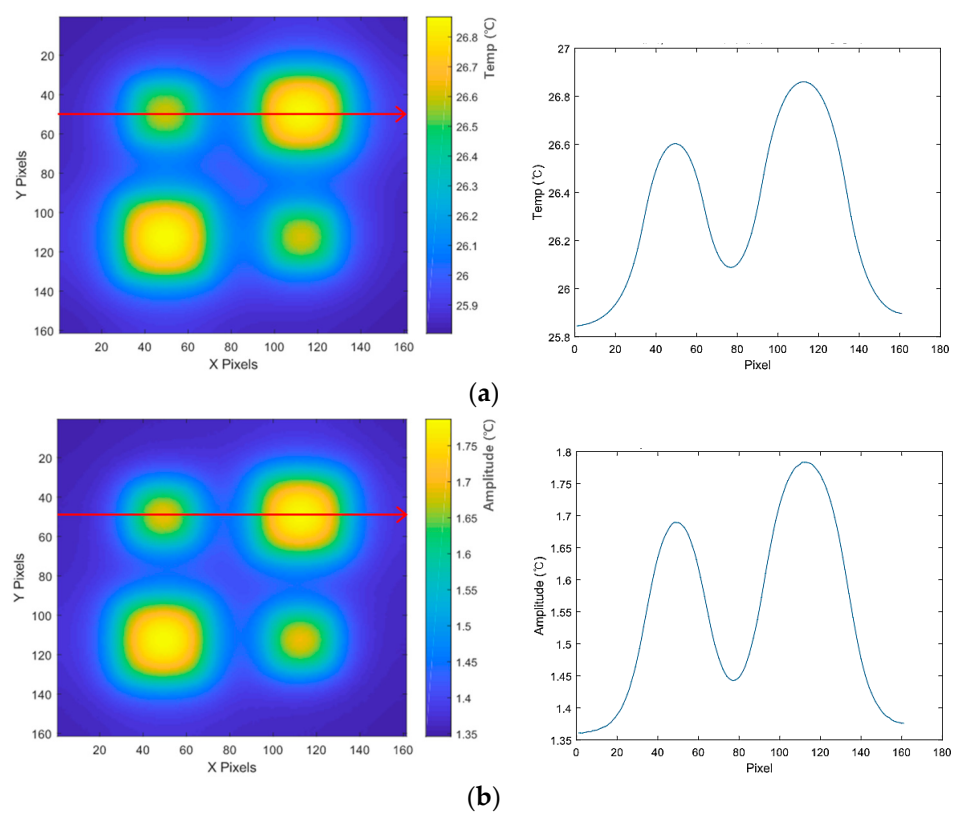


Figure 15. Cont.

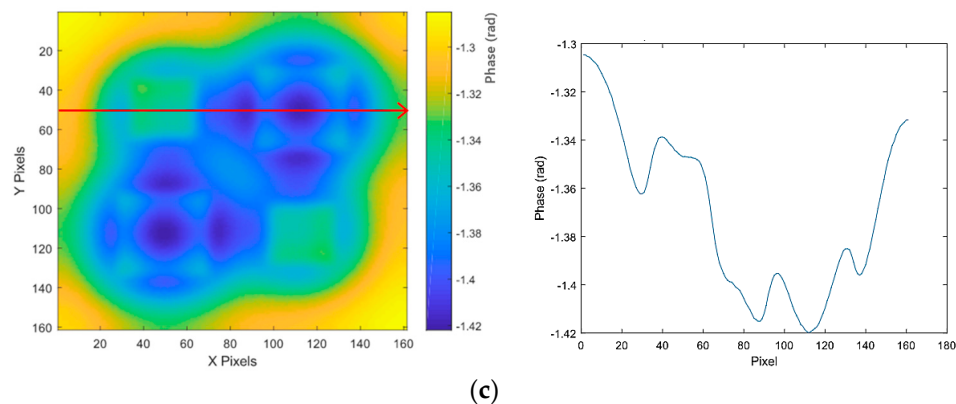


Figure 15. Analysis of the LIT simulation result in Case 3 (2 kW, 0.01 Hz): (a) temperature image and distribute (#74 frame, 148 s); (b) amplitude image and distribute (#58 step, 116–141–166–191 s); and (c) phase image and distribute (#58 step, 116–141–166–191 s). Left are thermography image of each type, right are result chart of arrow position and direction.

The detection ability of the active thermography test can generally be expected to be advantageous as the heat intensity is high and the time is long. However, if the performance of the flaw detector (temperature resolution, etc.) is good and the heat flux can be delivered evenly, it is estimated that good detection ability can be secured with less heat energy and test time, as shown in this simulation result.

5.3. Analysis of Experiments: Thermography

For the LIT thermography data obtained under the four test conditions through the CLP mockup specimen, the thermography image of the comparative analysis time was extracted, and the SNR for each ROI was calculated by analyzing the same method and procedure as the simulation. Figure 16a–c is a graph showing the temperature, amplitude, and phase SNR for each test based on the selected comparative analysis time. Figure 17a–c shows the temperature, amplitude, and phase images of Test 3 as an example.

As a result, it showed lower SNR compared to the simulation in all mockup test conditions. In addition, in the case of the phase image, the proportionality between the size of the concrete void and the SNR was prominent, whereas the proportionality was not found in the temperature and amplitude images.

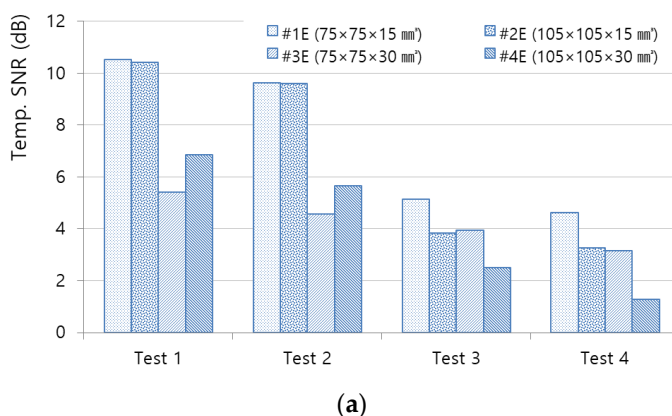


Figure 16. Cont.

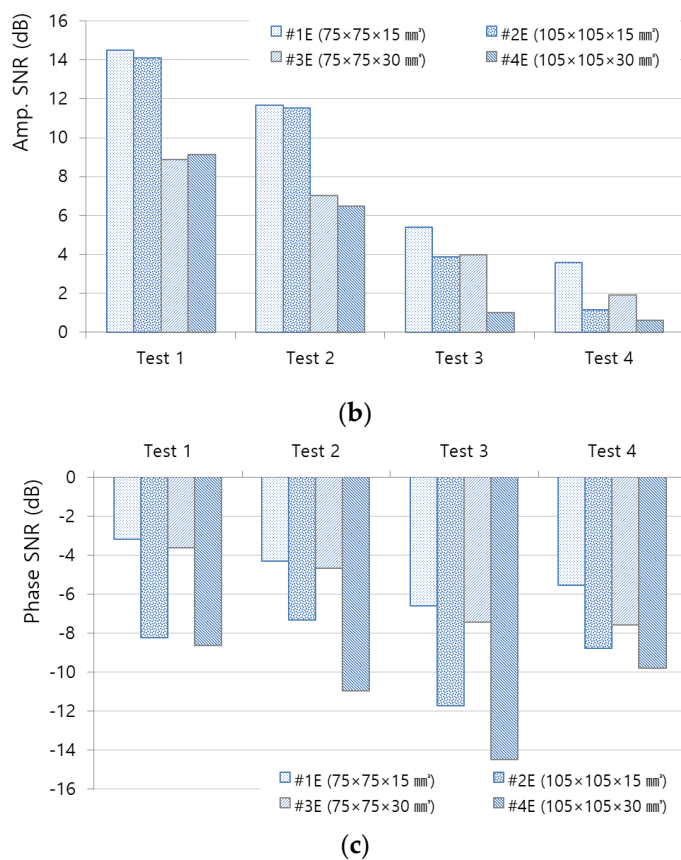


Figure 16. Comparison of CLP mockup experiment results by test condition: (a) temperature SNR (#925 frame); (b) amplitude SNR (#725 step); and (c) phase SNR (#725 step).

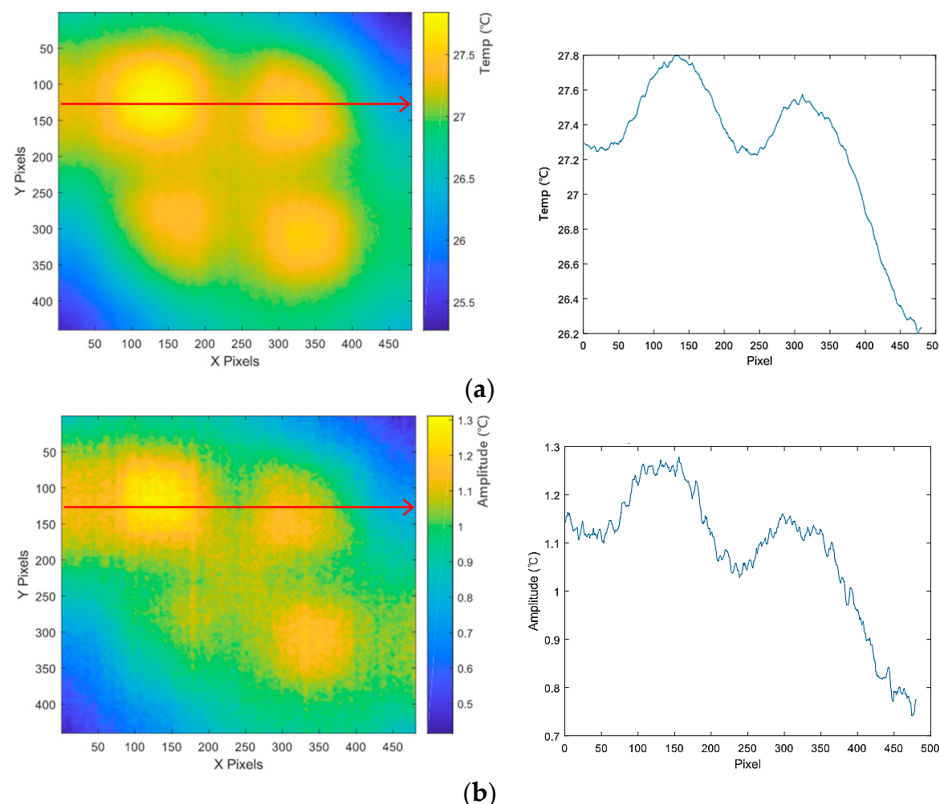


Figure 17. Cont.

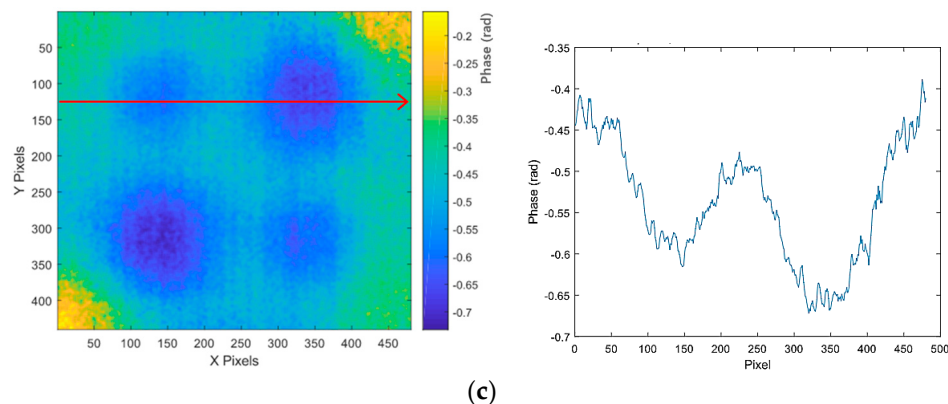


Figure 17. Analysis of LIT experiments results in Test 3 condition (2 kW, 0.01 Hz): (a) temperature image and distribute (#925 frame, 148 s); (b) amplitude image and distribute (#725 step, 116–141–166–191 s); and (c) phase image and distribute (#725 step, 116–141–166–191 s).

The hot spot effect of the halogen lamp, which is determined to be the cause, results in an unequal distribution of heat energy provided to the test subject. Additionally, unlike temperature and amplitude images, phase images are judged to be effective in overcoming the effects of uneven energy. In addition, even if the output of the lamp is nominally the same, it can be seen that the actual heat energy delivered to the inspection object is different, and the effect of the NETD of the IR camera and the noise in the test environment needs to be considered.

5.4. Comparative Analysis of Simulation and Experiment Results

As can be seen in this study, simulation of LIT and confirmation of EDP can be useful means for detecting the concrete voids on the CLP backside and for setting the evaluation and criteria. In the case of simulation, as shown in Figures 14 and 15, the SNR of the void was higher than 30 dB in all cases, and it is expected that the detection of concrete voids on the CLP backside will be smooth. In the case of the experiment, as shown in Figures 16 and 17, the temperature and amplitude images showed irregular and low SNR regardless of the size of the void, and it was possible to secure an identifiable SNR only in the phase image. This is thought to be the effect of the uneven heat load of the halogen lamp. As can be seen in the simulation and phase images of an experiment, the SNR value of concrete voids has a large effect in proportion to the void area, but the effect by depth is very small.

6. Conclusions and Future Works

This study is a case study on the LIT thermography inspection technique for the concrete voids on the back of the CLP of the nuclear power plant containment building. First, design/manufacture CLP mockup specimens containing four sizes of concrete voids. In the first step, a FEM model identical to the shape of the specimen was built, and thermography was replicated and analyzed through LIT simulation, considering four cases. As a second step, the LIT test under four conditions was run on the mockup specimen, and the obtained thermography was analyzed to compare/analyze the difference between the simulation and test results. As a result, the following conclusions were obtained:

1. Simulation through FEM can simulate thermography testing for LIT flaw detection conditions, and through simulated thermography analysis, EDP that can detect concrete voids can be confirmed and the ‘comparative analysis point’ can be derived and utilized;
2. In the case of the simulation, it was expected that the detection of concrete voids on the back of the CLP would be smooth with the LIT inspection technology, as it showed high detection and resolution in all cases;

3. In the actual test, detection and resolution were confirmed only in the phase image due to the influence of the hot spot and uneven heat energy transfer by the halogen lamp, but the temperature and amplitude images were not sufficient. Therefore, it is judged that the phase image is effective in overcoming the effect of uneven heat addition;
4. The proportionality between the concrete void size and the SNR was found to be significantly influenced by the void area, but the effect of the depth was minimal.

In the future, it is expected that concrete voids can be inspected more effectively if stronger energy is applied evenly to the CLP surface without a hot spot in the inspection condition of the concrete voids on the CLP backside. Therefore, we will consider device and software solutions to solve the problem of non-uniform heat addition, analyze the effect of improvement through problem solving, and report the results.

Author Contributions: Conceptualization, C.K.; methodology, C.K., Y.C. and W.K.; software, C.K., S.K. and Y.C.; validation, C.K. and Y.C.; formal analysis, C.K. and Y.C.; investigation, C.K. and S.K.; resources, C.K. and W.K.; data curation, Y.C.; writing—original draft preparation, C.K., S.K. and Y.C.; writing—review and editing, O.K. and W.K.; visualization, C.K. and S.K.; supervision, O.K.; project administration, C.K.; funding acquisition, C.K. and W.K. All authors have read and agreed to the published version of the manuscript.

Funding: This work was supported by a project for Industry-University-Research Collaboration R&D funded by the Korea Ministry of SMEs and Startups in 2023 (RS-2023-00224854).

Institutional Review Board Statement: Not applicable.

Informed Consent Statement: Not applicable.

Data Availability Statement: Not applicable.

Acknowledgments: This study received administrative and technical support from enesG, and we are grateful for all support. All authors consent to acknowledgments.

Conflicts of Interest: The authors declare no conflict of interest.

References

1. Workman, G.L.; Moore, P.O. Nondestructive Testing Overview. In *Nondestructive Testing Handbook Series III*, 3rd ed.; American Society for Nondestructive Testing: Columbus, OH, USA, 2012; Volume 10, pp. 2–13.
2. Umap, V.S.; Rao, Y.R.M. Application of Non-destructive Testing (NDT) Techniques on Reinforced Concrete Structure: A Review. *Int. J. Res. Appl. Sci. Eng. Technol.* **2023**, *11*, 817–824. [[CrossRef](#)]
3. Rahammer, M.; Kreutzbruck, M. Fourier-transform vibrothermography with frequency sweep excitation utilizing local defect resonances. *NDTE Int.* **2017**, *86*, 83–88. [[CrossRef](#)]
4. Tran, Q.H.; Han, D.; Kang, C.; Haldar, A.; Huh, J. Effects of Ambient Temperature and Relative Humidity on Subsurface Defect Detection in Concrete Structures by Active Thermal Imaging. *Sensors* **2017**, *17*, 1718. [[CrossRef](#)] [[PubMed](#)]
5. Ciampa, F.; Mahmoodi, P.; Pinto, F.; Meo, M. Recent Advances in Active Infrared Thermography for Non-Destructive Testing of Aerospace Components. *Sensors* **2018**, *18*, 609. [[CrossRef](#)] [[PubMed](#)]
6. Huh, J.; Mac, V.H.; Tran, Q.H.; Lee, K.-Y.; Lee, J.-I.; Kang, C. Detectability of Delamination in Concrete Structure Using Active Infrared Thermography in Terms of Signal-to-Noise Ratio. *Appl. Sci.* **2018**, *8*, 1986. [[CrossRef](#)]
7. Doshvarpassand, S.; Wu, C.; Wang, X. An Overview of Corrosion Defect Characterization using Active Infrared Thermography. *Infrared Phys. Technol.* **2019**, *96*, 366–389. [[CrossRef](#)]
8. Laureti, S.; Rizwan, M.K.; Malekmohammadi, H.; Burrascano, P.; Natali, M.; Torre, L.; Rallini, M.; Puri, I.; Hutchins, D.; Ricci, M. Delamination Detection in Polymeric Ablative Materials using Pulse-Compression Thermography and Air-Coupled Ultrasound. *Sensors* **2019**, *19*, 2198. [[CrossRef](#)]
9. Seelan, P.J.; Dulieu-Barton, J.M.; Pierron, F. Microstructural Assessment of 316L Stainless Steel Using Infrared Thermography Based Measurement of Energy Dissipation Arising from Cyclic Loading. *Mech. Mater.* **2020**, *148*, 103455. [[CrossRef](#)]
10. Moskovchenko, A.; Vavilov, V.; Švantner, M.; Muzika, L.; Houdková, Š. Active IR Thermography Evaluation of Coating Thickness by Determining Apparent Thermal Effusivity. *Materials* **2020**, *13*, 4057. [[CrossRef](#)]
11. Milovanović, B.; Gašić, M.; Gumbarević, S. Principal Component Thermography for Defect Detection in Concrete. *Sensors* **2020**, *20*, 3891. [[CrossRef](#)]
12. Garrido, I.; Solla, M.; Lagüela, S.; Fernández, N. IRT and GPR Techniques for Moisture Detection and Characterisation in Buildings. *Sensors* **2020**, *20*, 6421. [[CrossRef](#)]

13. Wei, Q.; Han, M.; Zhu, J.; Zhuo, L.; Huang, J.; Li, W.; Xie, W. Experimental and numerical investigation on detection fatigue crack in metallic plate by vibro-thermography. *Infrared Phys. Technol.* **2022**, *126*, 104347. [[CrossRef](#)]
14. Nuclear Safety and Security Committee. *Result of Inspection of the Root Cause of Voids in the Containment Building of Hanbit Units 3 and 4*; 162ed Report No. 1; NSSC: Seoul, Republic of Korea, 2022; pp. 1–10. Available online: https://www.nssc.go.kr/ajaxfile/FR_SVC/FileDown.do?GBN=X01&BOARD_SEQ=5&SITE_NO=2&BBS_SEQ=46152&FILE_SEQ=1 (accessed on 7 May 2023).
15. Nuclear Safety and Security Committee. *Status of Special Inspection of Nuclear Power Plant Structures and Future Plans*; 105th Other Report; NSSC: Seoul, Republic of Korea, 2019; pp. 1–12. Available online: https://www.nssc.go.kr/ajaxfile/FR_SVC/FileDown.do?GBN=X01&BOARD_SEQ=5&SITE_NO=2&BBS_SEQ=45575&FILE_SEQ=22884 (accessed on 7 May 2023).
16. Maldague, X. *Theory and Practice of Infrared Technology for Nondestructive Testing*; Wiley-Interscience: Hoboken, NJ, USA, 2001; ISBN 978-0-471-18190-3.
17. Shrestha, R.; Kim, W. Evaluation of Coating Thickness by Thermal Wave Imaging: A Comparative Study of Pulsed and Lock-in Infrared Thermography—Part I: Simulation. *Infrared Phys. Technol.* **2017**, *83*, 124–131. [[CrossRef](#)]
18. Lee, S.; Chung, Y.; Kim, C.; Shrestha, R.; Kim, W. Thermographic Inspection of CLP Defects on the Subsurface Based on Binary Image. *Int. J. Precis. Eng. Manuf.* **2022**, *23*, 269–279. [[CrossRef](#)]
19. Shrestha, R.; Kim, W. Evaluation of Coating Thickness by Thermal Wave Imaging: A Comparative Study of Pulsed and Lock-in Infrared thermography—Part II: Experimental Investigation. *Infrared Phys. Technol.* **2018**, *92*, 24–29. [[CrossRef](#)]
20. Vavilov, V.P.; Maldague, X.P.V.; Moore, P.O. Infrared and Thermal Testing: Heat Transfer. In *Nondestructive Testing Handbook Series III*, 3rd ed.; Maldague, X.P.V., Moore, P.O., Eds.; American Society for Nondestructive Testing: Columbus, OH, USA, 2001; pp. 54–86.
21. Meola, C.; Carlonmagno, G.M. Recent Advances in the use of Infrared Thermography. *Meas. Sci. Technol.* **2004**, *15*, 27–58. [[CrossRef](#)]
22. Ravichandran, A. Spatial and temporal modulation of heat source using light modulator for advanced thermography. Master’s Thesis, Missouri University of Science and Technology, Rolla, MO, USA, 2015; pp. 23–24.
23. Hernandez-Valle, S.; Peters, K. Numerical Simulation of Phase Images and Depth Reconstruction in Pulsed Phase Thermography. *Meas. Sci. Technol.* **2015**, *26*, 115602. [[CrossRef](#)]
24. Kim, M.-J.; Lee, J.-S.; Ko, S.-J.; Kang, S.-S.; Kim, J.-H.; Kim, D.-H.; Kim, C. Evaluation of Image Quality using ATS-539 Phantom and SNR in the Ultrasonographic Equipment. *J. Korea Contents Assoc.* **2013**, *13*, 284–291. [[CrossRef](#)]
25. Osama, K. Fundamentals of Heat Exchangers. *Int. J. Res. Comput. Appl. Robot.* **2018**, *6*, 1–11.
26. Kim, C.Y.; Chung, Y.J.; Kim, W.T. Optimization Method for Evaluating Essential Factors of Plate Backside Thinning Defects using Lock-in Thermography. *J. Korean Soc. Nondestruct. Test.* **2020**, *40*, 452–459. [[CrossRef](#)]
27. Ciorau, P. Comparison Between –6 DB and –12 DB Amplitude Drop Techniques for Length Sizing. *E-J. Nondestruct. Test.* **2011**, *16*. Available online: <https://www.ndt.net/?id=11175> (accessed on 7 May 2023).

Disclaimer/Publisher’s Note: The statements, opinions and data contained in all publications are solely those of the individual author(s) and contributor(s) and not of MDPI and/or the editor(s). MDPI and/or the editor(s) disclaim responsibility for any injury to people or property resulting from any ideas, methods, instructions or products referred to in the content.